Bioinspired Triboelectric Nanogenerators as Self-Powered Electronic Skin for Robotic Tactile Sensing

Guo Yao, Liang Xu, Xiaowen Cheng, Yangyang Li, Xin Huang, Wei Guo, Shaoyu Liu, Zhong Lin Wang,* and Hao Wu*

Electronic skin (e-skin) has been under the spotlight due to great potential for applications in robotics, human–machine interfaces, and healthcare. Meanwhile, triboelectric nanogenerators (TENGs) have been emerging as an effective approach to realize self-powered e-skin sensors. In this work, bioinspired TENGs as self-powered e-skin sensors are developed and their applications for robotic tactile sensing are also demonstrated. Through the facile replication of the surface morphology of natural plants, the interlocking microstructures are generated on tribo-layers to enhance triboelectric effects. Along with the adoption of polytetrafluoroethylene (PTFE) tinny burrs on the microstructured tribo-surface, the sensitivity for pressure measurement is boosted with a 14-fold increase. The tactile sensing capability of the TENG e-skin sensors are demonstrated through the characterizations of handshaking pressure and bending angles of each finger of a bionic hand during handshaking with human. The TENG e-skin sensors can also be utilized for tactile object recognition to measure surface roughness and discern hardness. The facile fabrication scheme of the self-powered TENG e-skin sensors enables their great potential for applications in robotic dexterous manipulation, prosthetics, human–machine interfaces, etc.

1. Introduction

With the recent development of flexible and stretchable electronics,[1–3] electronic devices mimicking human skin, i.e., Electronic Skin (e-skin),[4–6] have attracted significant research efforts due to the potential applications in robotics, human–machine interfaces, as well as healthcare.[7–9] E-skin sensors enable the detection and monitoring of proximity, pressure, strain, temperature, etc., or simultaneously monitoring multiple stimuli due to the capability of multimode sensing.[10–12] In contrary to conventional sensors, which are based on rigid substrate and functional materials, the flexible and stretchable nature of e-skin sensors demand the development of stretchable materials, structural design and corresponding fabrication schemes to achieve device flexibility or stretchability.[13,14] In the meantime, measurement sensitivity is also a critical metric for e-skin sensors to imitate the sensitive perception capability of human skin. To address those challenges, flexible or stretchable sensors based on capacitance,[15] piezoresistive,[16] optical or photonic effects[17] have been extensively investigated. However, capacitive and piezoresistive sensors require external power supply, which may be challenging to achieve for flexible systems.[18] Although piezoelectric sensors possess the merit of self-powering characteristic, the low electrical outputs limit their detection range and sensitivity.[19] Meanwhile, triboelectric effect has been merging as a new sensing mechanism for e-skin sensors.[20–22] Through the mechanism of triboelectrification and electrostatic induction, triboelectric nanogenerators (TENGs) can generate electrical signals and the magnitude of those signals can be correlated to the intensity of external stimuli, which endows TENG sensors with the feature of being self-powered.[23,24] In addition to the self-powered features, the sensitivity and measurement range of TENG based sensors can be enhanced or modulated through modifications of surface conditions, device mode or structures, etc.[25–28] Furthermore, a wide range of flexible or stretchable materials can be adopted for the fabrication of TENGs, enabling TENGs as advantageous candidates for the development of e-skin sensors.[29] Indeed, TENG as an effective approach to realize e-skin sensors has been verified

G. Yao, X. Cheng, Y. Li, X. Huang, W. Guo, S. Liu, Prof. H. Wu
Flexible Electronics Research Center
School of Mechanical Science and Engineering
Huazhong University of Science and Technology
Wuhan, Hubei 430074, China
E-mail: hwu16@hust.edu.cn
Prof. L. Xu, Prof. Z. L. Wang
Beijing Institute of Nanoenergy and Nanosystems
Chinese Academy of Sciences
Beijing 100083, China
E-mail: zhong.wang@mse.gatech.edu
Prof. L. Xu, Prof. Z. L. Wang
School of Nanoscience and Technology
University of Chinese Academy of Sciences
Beijing 100049, China
Prof. Z. L. Wang
School of Materials Science and Engineering
Georgia Institute of Technology
Atlanta, GA 30332-0245, USA

by a number of studies. For instance, Lin et al. demonstrated a TENG sensor array for self-powered pressure detection and theoretically proved that TENG could be applied for both static and dynamic pressure measurements,[30] Yang et al. developed a single electrode TENG for self-powered sensing of human touch.[31] Recently, Pu et al. presented an ultrastretchable and transparent TENG (stretchability of 1160% and transparency of 96.2% for visible light) e-skin sensor for tactile sensing.[32] Ren et al. developed a fully elastic TENG e-skin sensor which could detect both normal and tangential forces.[33]

Meanwhile, bioinspired design has been an attractive strategy for the enhancement of e-skin sensor measurement sensitivity. As an example, human skin has been under scrutiny as a model for bioinspired design.[34] The fingerprint patterns on skin enable sensitive perception of fine stimuli through amplification of vibrotactile signals,[35] while the interlocking microstructures between the epidermal and dermal layers can amplify and efficiently transfer tactile stimuli to cutaneous mechanoreceptors.[36,37] Park et al. fabricated the fingerprint-like patterns and interlocking microstructures in ferroelectric film, which significantly enhanced the piezoelectric, pyroelectric, and piezoresistive sensing of pressure and temperature.[38] Boutry et al. proposed an interlocking structure for the fabrication of capacitive e-skin sensors to distinguish the direction of applied pressure.[39] However, the fabrication methods adopted by those studies typically involved sophisticated fabrication procedures including lithography and etching. An alternative and efficient method to achieve bioinspired microstructures for

sensitivity enhancement is to replicate the hierarchical structures of natural plants.[40,41] Here we report the fabrication of bioinspired TENGs as self-powered e-skin sensors for robotic tactile sensing. Specifically, we fabricate the interlocking structures in the triboelectric layers through the facile replication of the cone-like array microstructures of the *Calathea zebrine* leaf. With the interlocking microstructures and the formation of polytetrafluoroethylene (PTFE) tinny burrs on the tribo-layer, the pressure measurement sensitivity is increased to fourteen fold. Due to the flexibility, the self-powered TENG e-skin sensor can be easily attached onto a bionic hand to verify its applications in robotics. The human–robot handshaking as a representative human–machine interaction is characterized through the measurements of handshaking pressure distribution and bending angles of each finger of the bionic hand. We further demonstrate the tactile sensing capability of the TENG e-skin sensor through the detection of surface roughness and distinction of object hardness. With the high sensitivity enabled by the bioinspired structure design, the TENG e-skin sensors are promising for applications in robotic dexterous manipulation, prosthetics, and human–machine interfaces.

2. Results and Discussion

Figure 1 depicts a schematic structure of the TENG e-skin sensor. The sensor consists of four layers, including a shielding layer, a triboelectric layer with silver nanowires (AgNWs) on
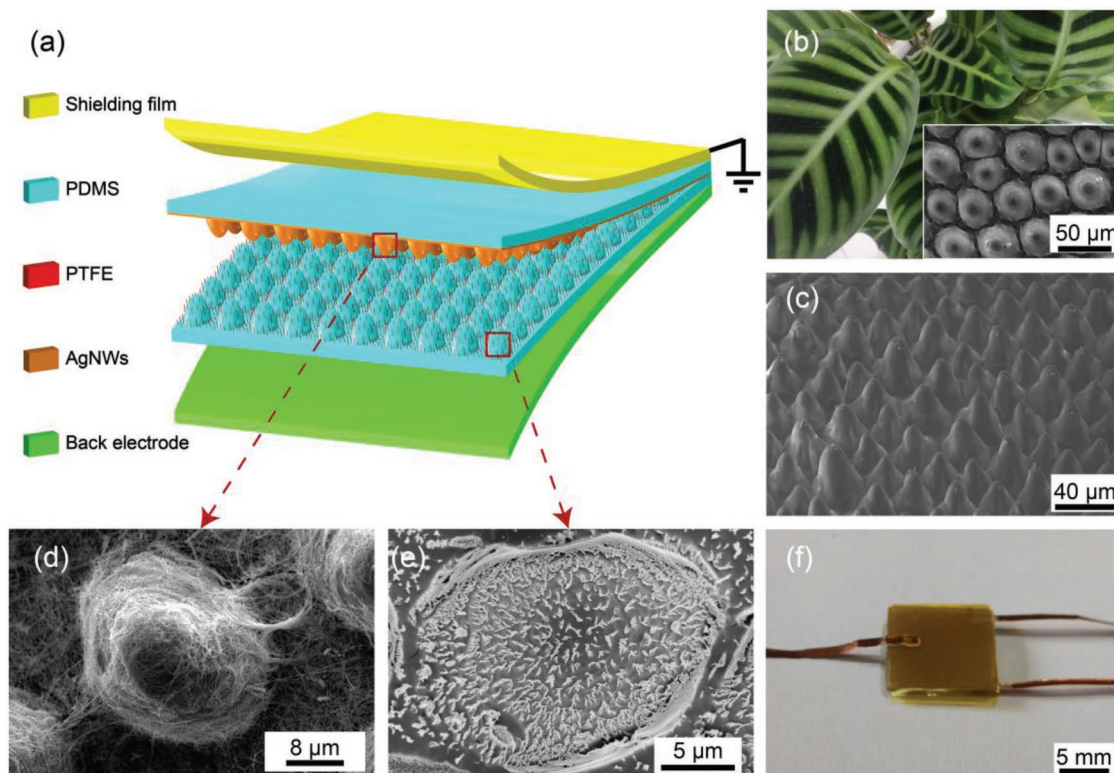

Figure 1. Structural illustration of the TENG e-skin sensor. a) Schematic diagram of the TENG e-skin sensor structure. b) Photograph of the *C. zebrine* leaf. c) Micromorphology of biomimetic microstructures. d) Micromorphology of silver nanowires sprayed on PDMS pillar e) SEM image of the PTFE tiny burrs on PDMS surface. f) Photograph of the TENG e-skin sensor.

the microstructured PDMS surface, the other triboelectric layer composed of PTFE tiny burrs on the microstructured PDMS surface, and a back electrode layer. The shielding layer is adopted to effectively screen electrostatic interferences to ensure measurement accuracy, as recommended by previous study.[33] The cone-like PDMS microstructures on both the triboelectric layers are fabricated through the replication of the surface of the *C. zebrine* leaf, which demonstrates relatively uniform cone-like morphology, as shown in Figure 1b and inset. The first molding of the original *C. zebrine* leaf allows the fabrications of PDMS with reverse patterns, and another molding process on the resultant PDMS patterns yields the replication of the array of cone morphology on PDMS substrate. Details of the fabrication processes are elaborated in the Experimental Section. This two-step templating approach allows facile replication of the array of the cone-shape microstructures, as shown in Figure 1c. The replicated microcones have an average height of ≈25.7 µm with an average base diameter of ≈25.4 µm, and an average inter-cone distance of ≈33.6 µm. Under applied pressure, the arrays of cone-like microstructures on top and bottom triboelectric layers can form interlocked contact, leading to enhanced frictional areas between the two layers. Due to the percolation network in silicone matrix to achieve enhanced stretchability, AgNWs have been widely adopted to fabricate electrodes and interconnects in stretchable electronics.[42] In this study, AgNWs were spray coated onto PDMS substrate to form the top shielding layer and back electrode, as well as the triboelectric layer on the microstructured PDMS surface. As shown in Figure 1d, the AgNWs conductive network can be clearly observed on the microcone structure. Meanwhile, since PTFE has been known as an effective tribo-negative material,[29] PTFE tiny burrs in the size of micron or submicron were generated on top of microstructured PDMS surface through evaporation and reactive ion etching (RIE) to enhance triboelectric effect, as shown in Figure 1e. It is pointed out that the

formation of PTFE tiny burrs on the PDMS substrate is advantageous as they do not compromise the stretchability of the substrate. Therefore, the adoptions of silicone substrate, AgNWs and PTFE tiny burrs enable the stretchability of the overall TENG electronic skin sensor. The photograph of the overall device is shown in Figure 1f. Figure S1 (Supporting Information) illustrates the fabrication steps of the sensor and process details can be found in the Experimental Section.

The working mechanism of the TENG e-skin as self-powered pressure sensor is based on triboelectric effect and electrostatic induction, as illustrated in **Figure 2**a. Under applied pressure, the top and bottom triboelectric layers will be forced to contact and the interlocking structures formed by the cone-like morphology leads to increased frictional contact. Due to the different abilities of electron affinities, equal amount of positive and negative charges are generated on the AgNWs of the top tribo-layer and PTFE burrs/PDMS microstructures of the bottom tribo-layer, respectively (Figure 2aI). When the external pressure is reduced and the two tribo-layers are separated, the AgNWs tribo-layer will have higher electric potential, while the back electrode of the bottom tribo-layer will have lower electric potential. The electrostatic induction due to the difference in electric potentials drives the electrons to flow from the back electrode to the top AgNWs tribo-layer, leading to electric current flowing from top to bottom (Figure 2aII). This process proceeds until the external pressure reduces to zero without further variation, an electric equilibrium is achieved and the charge transfer stops (Figure 2aIII). When the external pressure is applied again, electricity will flow in the reverse direction (Figure 2aIV), completing a full cycle of electricity generation. To investigate the performances of the TENG e-skin sensor for pressure measurements, a motorized Z-stage was used in combination with a force gauge to apply well-defined pressure. The external pressure and electrical outputs were controlled and recorded simultaneously. Under cyclic loading pressure of
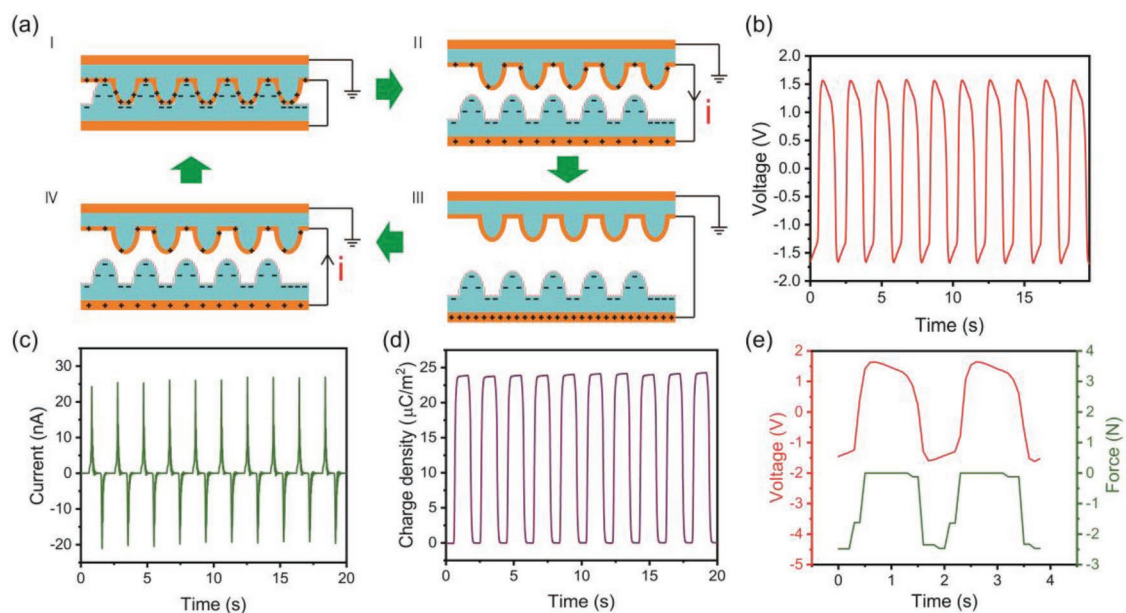
Figure 2. Detection of normal force. a) Working principle for detecting normal force. b–d) Open circuit voltage, short circuit current and transferred charges of the TENG e-skin sensor under a pressure of 25 kPa. e) Synchronized force input and voltage output during cyclic loading of 25 kPa.

25 kPa, the open circuit voltage (V_{oc}), short circuit current I_{sc} and transferred charge density σ_{tr} of the sensor are shown in Figure 2b–d, respectively. While all the output signals demonstrated excellent repeatability, the maximum ΔV_{oc}, peak I_{sc} and maximum σ_{tr} reached 3.14 V, 26.29 nA, and 23.98 μC m^{-2}, respectively. The ΔV_{oc} is defined as $V_{oc} - V_{ocnp}$, where V_{ocnp} is the negtive peak of the voltage signal. As one of the output characteristics of the contact-separation mode TENGs, the maximum ΔV_{oc} increases as the separation distance increases, as shown in Figure S2 (Supporting Information). The synchronized force input and open circuit voltage between the back electrode and top tribo-layer are shown in Figure 2e. It is noticed that the voltage reached the maximum value when the applied force was fully retracted which corresponds to the largest separation distance of the two tribo-layers. The voltage decreased when the force was applied again and reached maximum value with reverse sign when the two tribo-layers completely contacted again (Figure 2e).

It is noted that the combination of the bioinspired interlocking microstructures of cone-like morphology and the formation of PTFE tiny burrs significantly enhanced the triboelectrification during contact of the tribo-layers, leading to higher sensitivity for pressure measurements. TENG sensors of different microstructures and surface conditions were fabricated and their performances as pressure sensors were evaluated, as shown in **Figure 3**. Five types of sensors of the same size were compared to systematically investigate the impact of

tribo-layer surface conditions on sensitivity, including sensors of flat AgNWs tribo-layer and flat PDMS tribo-layer (Flat), flat AgNWs tribo-layer and PDMS tribo-layer with cone-like microstructures (Flat + Microstructures), interlocking AgNWs and PDMS tribo-layers with cone-like microstructures on both surfaces (Interlocking), interlocking AgNWs and PTFE tribo-layers with PTFE film on the cone-like surface (Interlocking + PTFE film), as well as interlocking AgNWs and PDMS/PTFE tribo-layers with PTFE tiny burrs on the cone-like surface (Interlocking + PTFE burrs). The horizontal axis of Figure 3a represents the maximum ΔV_{oc} of the sensor output under applied pressure, and the pressure measurement sensitivity of those five different sensors are calculated as 9.08, 20.59, 59.65, 17.5, and 127.22 mV kPa^{-1}, respectively, in the pressure range of 5–50 kPa. The interlocking structures of AgNWs and PDMS tribo-layers lead to larger effective contact areas than those with flat surfaces, resulting in higher measurement sensitivity. However, the sensor with interlocking structures and PTFE film demonstrated relatively low sensitivity. This is potentially due to the fact that the relatively thick film ($\approx$150 μm) of PTFE with large modulus (860 MPa–1.6 GPa[43,44]), which is about four orders of magnitude larger than PDMS ($\approx$1–3 MPa),[45] results in significantly increased stiffness of the microstructures which prohibits the interlocking contact under external load. Therefore, the formation of PTFE tiny burrs through RIE is critical for improved measurement sensitivity after the deposition of the PTFE film, as the tiny burrs distributed on the cone-like
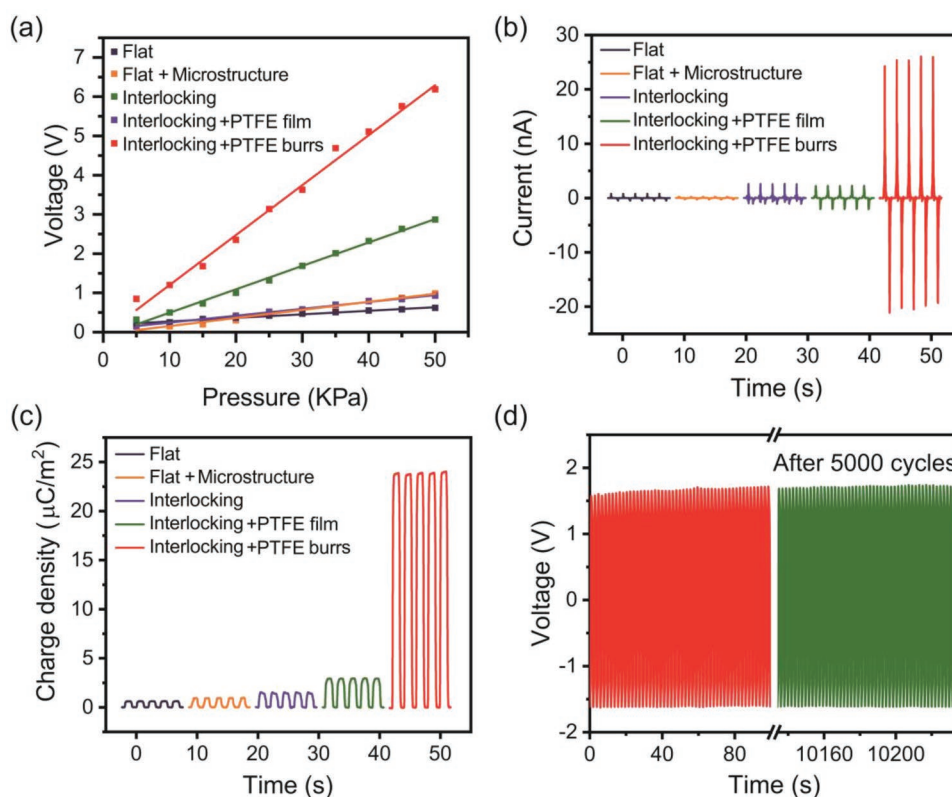

Figure 3. Performances of the TENG e-skin sensor. a) Sensitivity comparisons of sensors with different microstructures and surface condition. b,c) Current and charge density output of different sensors during cyclic loading with maximum pressures of 25 kPa. d) Durability of the sensor tested for 5000 cycles under a pressure of 25 kPa.

PDMS structures can enhance triboelectric effect without increasing the overall structure stiffness. Therefore, the e-skin sensors with interlocking microstructures and PTFE burrs have much higher sensitivity than the rest. The enhancement of triboelectric effect is also confirmed by the short circuit current I_{sc} and transferred charge density σ_{tr} of the sensors under 25 kPa of cyclic loading pressure, as shown in Figure 3b,c, respectively. It is clear that both I_{sc} and σ_{tr} are significantly boosted, i.e., about an order of magnitude increase was achieved compared with sensors with other designs, when the interlocking structures and PTFE burrs are adopted. It is pointed out that the present bio-inspired TENG e-skin sensor also possesses the advantage of high measurement sensitivity when compared with previously reported TENG pressure sensors of the similar device structure. For instance, the micropyramid array patterned triboelectric sensor presented by Jiang et al. demonstrated a sensitivity of only 2.82 ± 0.187 mV kPa^{-1},[46] while the hemispheres-array-structured TENG pressure sensor reported by Lee et al. achieved a sensitivity of ≈ 28.8 mV kPa^{-1}.[47] The better sensitivity is attributed to two reasons: i) the soft bioinspired interlocking microstructures enable the increase of effective frictional areas, which could cause a larger change in potential difference per unit area under external load; ii) the presence of the PTFE tiny burrs on the PDMS microstructures enhances the triboelectric effect as PTFE is one the most effective tribonegative materials. The bioinspired TENG e-skin sensor also demonstrates excellent durability and stability. Although slight wear of AgNWs on the PDMS pillar occurred (Figure S3, Supporting Information), the sensor output remained consistent without degradation after 5000 cycles of loading tests with loading pressure of 25 kPa at a frequency of 0.5 Hz, as shown in Figure 3d. The high durability of the sensor can be attributed to the elasticity of the interlocking microstructures and percolation network formed by the AgNWs in the device structure.

The bioinspired TENG e-skin sensor may also be applied to measure tangential sliding forces due to the presence of interlocking tribo-layers, as shown in Figure S4 (Supporting Information). The measurement mechanism is illustrated in Figure S4a (Supporting Information). When the two tribo-layers are in contact, equal amount of positive and negative charges are generated. Relative sliding motion of those two tribo-layers caused by the external tangential force will lead to the variation of contact areas and the resultant potential difference between the AgNWs tribo-layer and the back electrode, similar as the mechanism demonstrated in Figure 2a. For tangential sliding force of 1 N, the maximum ΔV_{oc} reached 0.012 V with a certain sliding displacement of 1 mm, and the simultaneously recorded tangential sliding force and the maximum ΔV_{oc} are presented in Figure S4b (Supporting Information). Larger tangential sliding force means larger friction and more triboelectric charges, resulting in higher value of V_{oc} under certain sliding displacement. The plot of the maximum ΔV_{oc} and tangential forces in Figure S4c (Supporting Information) indicates that they are highly linearly correlated in the force range of 0.5–2 N, which enables the measurement of tangential forces through the detection of V_{oc}. Due to the adoption of soft and stretchable PDMS substrate, the compliant nature of the interlocking microstructures facilitates the sliding motion and enable the e-skin sensor to work under sliding TENG mode for the measurement of tangential load.

The TENG e-skin sensors were integrated onto a bionic hand to demonstrate their applications for robotic tactile sensing. Handshaking between robotic dexterous manipulators and human has been considered as the representative scenario for human–machine interfaces,[48,49] as shown in **Figure 4**a. Due to the low thickness and flexible nature, the TENG e-skin sensors can be easily attached to the curvy surfaces of a bionic hand to measure handshaking pressure from human hands,
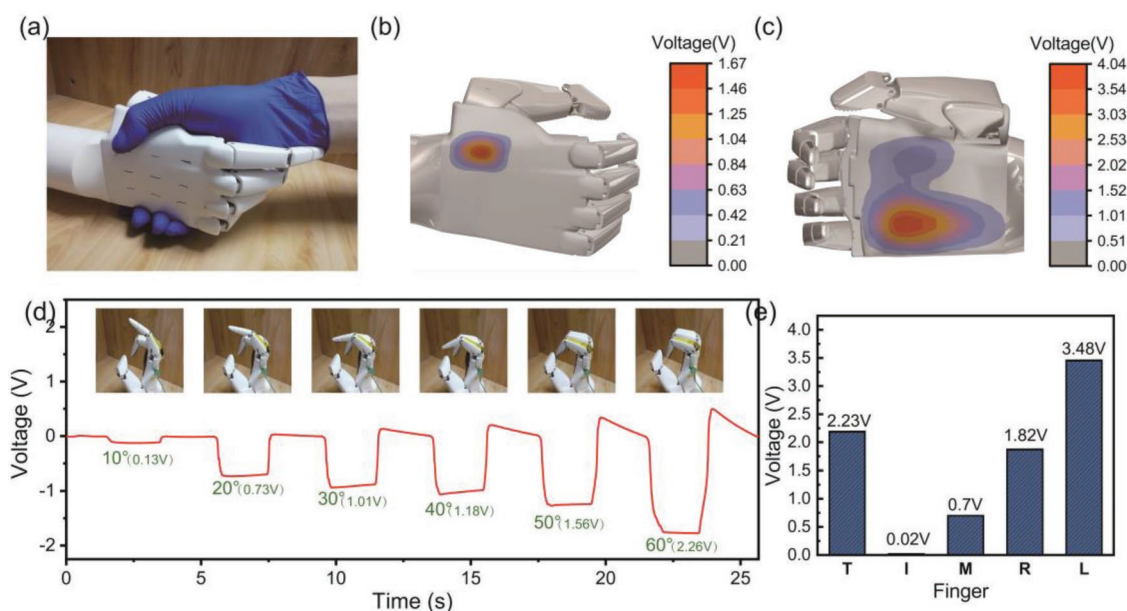

Figure 4. Tactile sensing of the triboelectric sensor through integration on a bionic hand. a) Photograph of human–robot handshaking. b,c) the voltage contour profiles on the back and palm of the bionic hand during handshaking. d) Real-time voltage signals in response to index finger gestures with different bending angles. e) Voltage signals in response to each finger gesture during human–robot handshaking.

**ADVANCED
SCIENCE NEWS**
www.advancedsciencenews.com

**ADVANCED
FUNCTIONAL
MATERIALS**
www.afm-journal.de

as well as the bending angle of each finger. To achieve those measurements, two 3×3 e-skin sensor arrays were attached to the front and back of the bionic hand and 5 sensors were attached to the finger joints to the palm, as shown in Figure S5 (Supporting Information). The contour maps of maximum ΔV_{oc} during handshaking were calculated based on the interpolation of the outputs from those 3×3 e-skin sensor arrays, as shown in Figure 4b,c. As expected, the contact pressure only occurred on the location of the human thumb on the back of the bionic hand. While the pressure map on the palm of the bionic hand indicates higher contact pressure occurred at the lower part of the palm, which are consistent with the pressure measurements from commercial thin film sensors (see Figure S6 in the Supporting Information). As shown in Figure 4d, the increase in the bending angle of the index finger of the bionic hand leads to the increase of maximum ΔV_{oc}, and the correlations between the bending angles and maximum ΔV_{oc} for all the five fingers are measured and plotted in Figure S7 (Supporting Information). Based on the maximum ΔV_{oc} measurements from each finger shown in Figure 4e, the bending angles of those five fingers during handshaking can be estimated to be 56°, 2°, 17°, 45°, and 58°, corresponding to thumb, index finger, middle finger, ring finger, and litter finger, respectively. It is noted that those measurements were obtained at normal humidity (relative humidity 49%) in laboratory environment. However, the decrease in voltage output was observed if the ambient relative humidity was increased to 70%, as shown in Figure S8 (Supporting Information), which was due to the

depletion of induced charged caused by the water layer formed on the surface of the tribo-layers.[50] The impact of humidity on the performances can be alleviated by effective packaging of the sensor to achieve humidity isolation.

Object recognition and characterizations are important elements for robotic tactile sensing to achieve interactions with human and environment and autonomous manipulation. The bioinspired TENG e-skin sensor was also applied for tactile object identification to evaluate the surface roughness and hardness. Figure S9 and Video S1 (Supporting Information) illustrate the experimental setup and procedures for the measurements of surface roughness, and details can be found in the Experimental Section. Sandpapers with different surface conditions were attached to a motorized stage and preloaded by a constant normal force. During the sliding process driven by the motorized stage, V_{oc} of the TENG e-skin sensor pressed against the surface of sandpapers was recorded. P400, P600, P1000, and P1400 sandpapers based on the standard of the Federation of European Producers of Abrasives (FEPA) were tested and their surface morphologies are shown in **Figure 5**a. It can be seen that the surface gets smoother as the grit size decreases. The V_{oc} data during the sliding process of each sandpaper are shown in Figure S10 (Supporting Information), indicating that rough surfaces generally cause larger variation of voltage output due to higher friction force. In the evaluation of surface texture through tactile sensing data, an effective approach for analyzing surface roughness is to compute the logarithm of the variance of the original signal measured by the tactile sensor.[51]
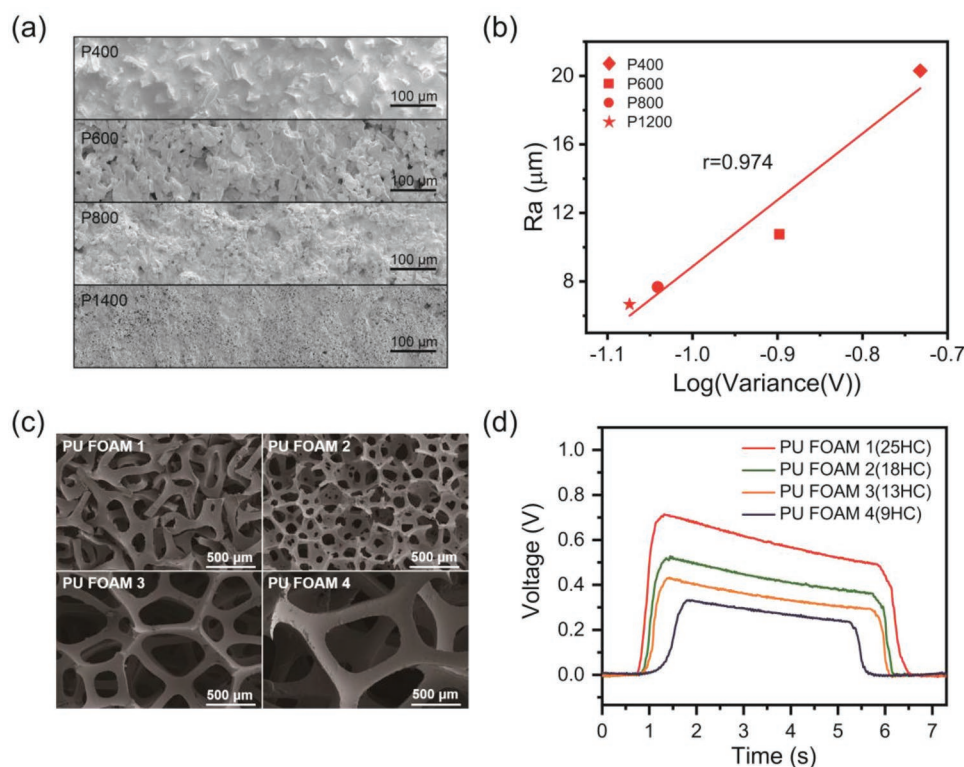
Figure 5. Perception of surface roughness and hardness. a) SEM images of the surface morphology of the test samples (sandpaper P400, P600, P800, P1400). b) Correlation between surface roughness of sandpaper and output signal (log(Variance(V)). c) SEM images of PU foams with different hardness. d) Comparisons of real-time voltage signals of the sensor during contact and separation with foam of different hardness.

Table 1. The comparisons of transduction mechanisms for e-skin sensors.[3,22,52]

Transduction Mechanism	Advantages	Disadvantages
Triboelectric	Self-powered; high sensitivity; high linearity; large range; sensitive to dynamic stimuli; facile fabrication; flexibility in materials selection	Sensitive to environment (humidity, etc.)
Piezoelectric	Self-powered; sensitive to dynamic stimuli; fast response	Drift in response overtime; unreliable static sensing; materials limitation (piezoelectric materials)
Capacitive	High sensitivity; low detection limit; fast response	Susceptible to interference; low signal magnitude (low signal to noise ratio)
Piezoresistive	High sensitivity at low pressure range; large range; fast response	Undesirable drift and hysteresis

The roughness average (Ra) measured by optical microscope versus the logarithm of the variance of the V_{oc} for each sample are shown in Figure S11 (Supporting Information). The Pearson correlation coefficient of those two groups of data is as high as 0.974 (Figure 5b), indicating close linear correlation of those two data sets. Therefore, the tactile sensing data from the TENG e-skin sensor can be conveniently adopted for quantitative analysis of surface roughness.

The hardness evaluation capability of the TENG e-skin sensor was investigated through distinguishing the hardness of Polyurethane (PU) foams of different microstructures. The difference in the size and density of the foam structural ribs leads to the difference in hardness, as shown in Figure 5c. As expected, PU foams with higher density of structural ribs demonstrated larger hardness, and the hardness of those four types of PU foams were measured to be 25, 18, 13 and 9, respectively, by a Shore durometer. The experimental procedures of hardness evaluation using the TENG e-skin sensor are depicted in Figure S12 and Video S2 (Supporting Information). PU foams of the same thickness were attached to the motorized stage to separate from and contact the TENG e-skin sensor, while the ΔV_{oc} of the sensor was recorded throughout the process. Before the tests, the PU foam and the TENG e-skin sensor were loaded by a constant normal force from the lower side, and the starting position of the linear motor was kept the same. Here, the soft foam had larger initial deformation than the hard foam due to its lower stiffness. In the process of separation by the motor, the foams would gradually restore to their original shape, accompanying by the load releasing and voltage rising. Complete separation of the foams and the sensor would produce a peak in the voltage signal, after which the signal would decrease slightly due to charge dissipation. The complete separation of softer foams occurs later than harder ones due to their larger initial deformation under the load which needs more upward motion of the motor. Thus the rise peak of ΔV_{oc} happened later for softer foams (Figure 5d). It was also noticed that soft foams had lower ΔV_{oc} peaks. This is due to their higher compliance to the shape of the e-skin sensor while loaded, which results in a worse contact state in the center of the arch-shape sensor, producing smaller signals. When the foam approaches the sensor again, ΔV_{oc} for softer foams decreases earlier as the foam and sensor contact sooner (Figure S12d, Supporting Information). Therefore, the hardness of these PU foams can be clearly distinguished through the comparisons of the rise rate and magnitude of ΔV_{oc}. The above tests demonstrate that our bio-inspired TENG e-skin sensor can discriminate object surface roughness and hardness, indicating its potential applications in robotic tactile sensing.

In fact, TENGs have been rapidly emerging as a very important transduction mechanism for the development of e-skin tactile sensors since its invention just a few years ago.[20] The comparisons of TENGs with other major transduction mechanisms are summarized in **Table 1**. The performances of the TENG e-skin sensors, such as sensitivity, measurement linearity and range, have been significantly improved since their first application as pressure sensors.[21,22] While the susceptibility to environmental factors such as humidity or electrostatic interference can be alleviated through effective shielding or device packaging, the unique characteristics of TENGs, such as the self-powered feature, facile fabrication schemes and flexibility in materials selection, will boost their widespread applications as e-skin sensors in robotic dexterous manipulation, prosthetics, human–machine interfaces, etc.

3. Conclusion

In summary, we present a bioinspired TENG e-skin sensor for applications in robotic tactile sensing. The bioinspired interlocking microstructures were achieved through facile replication of the array of cone-like morphology from the *C. zebrine* leaf surface. The adoption of the interlocking microstructures and PTFE tiny burrs on the tribo-layers significantly enhance the sensitivity of the TENG e-skin sensor. Due to the intrinsic flexibility, the e-skin sensor can be conveniently attached to a bionic hand to achieve tactile sensing for human–robot interaction, as well as to realize texture object recognition. It has been shown that the surface roughness of sandpapers could be quantitatively correlated to the measurement data of the TENG e-skin sensor. Furthermore, the TENG e-skin sensor can be applied to discriminate objects of different hardness. Due to the facile fabrication schemes and high sensitivity, the TENG e-skin sensor may have important applications in robotic dexterous manipulation, prosthetics, human–machine interfaces, and so on.

4. Experimental Section

Fabrication of Microstructured PDMS Substrate: Fresh *C. zebrine* leaf was washed with deionized water and then cut into rectangle. Leaf edge was cut away to avoid inconsistency of the surface microstructures. After dried by air blowing, the *C. zebrine* rectangle was fixed onto a glass substrate using 3M tapes. PDMS base (Sylgard 184, Dow Corning Co., Ltd) was mixed with the curing agent at a weight ratio of 10:1 and placed in a vacuum chamber for 20 min until bubbles disappeared. Next, the uncured PDMS was cast on the rectangular leaf. After curing at room

temperature for 48 h, it was peeled off as the template for the second molding process. To reduce the undesirable adhesion in the next second molding process, the molding template was subject to reactive ion etching (oxygen flow rate was 20 sccm, reaction pressure was 70 Pa, radio frequency power was 90 W, reaction time was 90 s) (Etchlab 200, SENTECH instruments GmbH) and hydrophobic treatment. Uncured PDMS was cast on the template and placed in a vacuum chamber for 20 min in order to eliminate bubbles. After curing at 90 °C for 1 h, the microstructured PDMS substrate was peeled off from the template, the thickness of the substrate was about 400 µm.

Fabrication of PTFE Tiny Burrs: A layer of PTFE film was deposited on the substrate by vacuum evaporation (BOX-RH400, SKY TECHNOLOGY DEVELOPMENT), and the thickness of the PTFE film was about 150 µm. Afterward, a 10 nm thick Au layer was sputtered onto the PTFE surface, which was used as a mask for the etching process. The sputtering power was 80 W and lasted for 1 min (TPR-450 PVD system). Subsequently, the sample was etched through reactive ion etching (ICP) for 5 min (Plasmalab system 100 ICP180). The reaction gas was 15.0 sccm Ar, 10.0 sccm O_2, and 30.0 sccm CF_4 in the ICP process. One power source of 400 W was used to generate a large density of plasma and another power of 100 W was used to accelerate the plasma ions. After the above procedures, the PTFE tiny burr were formed on the surface of the microstructured PDMS substrate.

Preparation of Flexible Electrodes and Sensor: AgNWs were purchased from Nanjing XFNANO Materials Tech Co., Ltd. The AgNWs solution was mixed with ethanol by a volume ratio of 1:20 to obtain a diluent. Spray coating was performed to prepare conductive AgNWs network by using an air gun. AgNWs were sprayed onto the back side of the microstructured PDMS substrate having the PTFE tiny burr layer as a back electrode, and sprayed onto the front and back sides of another microstructured PDMS substrate as a friction layer and a shielding layer, respectively. Subsequently, a copper foil was mounted on the edge of the AgNWs film by conductive silver paste and heated at 90 °C for 1 h as electrical contact. The two layers were bonded by nonconductive tapes at 90 °C. After the temperature dropped to room temperature, the device naturally formed an arch shape due to the elastic resilience of the PDMS, with an air gap presented for effective charge separation. Finally, the edges of two layers were bonded with kapton tape for encapsulation. The size of the devices was 1 cm^2.

Characterizations and Tactile Sensing Experiments: The microstructures of the *C. zebrine* leaf, silver nanowires sprayed on PDMS, PTFE tiny burrs, surface morphology of sandpaper and microstructures of PU foam were inspected by field-emission scanning electron microscopy (Nova NanoSEM 450,Czech and JEOL JSM-6701F, Japan). The electric signals of the triboelectric sensor were measured using a data acquisition card (USB-6218, National Instruments, USA) and an electrometer (Keithley 6514 system). The analog signals generated in the sensing system were converted to digital data for recording and analysis using LabVIEW (National Instruments, USA) and Matlab (Mathworks, USA). A force gauge (HP-50N by HANDPI) was used to record the force. The bionic hand with five fingers (each finger was controlled by a motor) was purchased from INSPIRE ROBOTS (model # DH5-031L). The motion of the bionic hand was controlled through a serial port by controlling the motor on each finger. For the measurements of surface roughness, the sandpapers were attached to a motorized stage and preloaded by a normal force of 1 N (calibrated by the force gauge), and the TENG e-skin sensor was installed in between the sandpaper and the force gauge. The sandpaper was driven by the motorized stage to move 1 mm with a maximum speed of 0.01 m s^{-1} and acceleration/deceleration of 0.01 m s^{-2}, and there was 300 ms pause at the end of each motion. The V_{oc} of TENG e-skin sensor was recorded during the process. The surface roughness Ra of sandpapers were measured using a laser scanning confocal microscope (Keyence, model VK-X200). Roughness at ten locations were measured for each sample to obtain statistical significance. For the measurements of hardness, the PU foams were purchased from caligen, UK (model 30 ppi) and cut into the same thickness of 10 mm. The hardness of the PU foams were measured by a Shore durometer (Raytech, model LX-C). During the experiment, the PU foam was attached to the motorized stage to separate from and contact the TENG e-skin sensor. The motor moved away from the TENG e-skin sensor at 0.01 m s^{-1}, then paused for 300 ms, followed by approaching the sensor at 0.01 m s^{-1} to achieve full contact.

Supporting Information

Supporting Information is available from the Wiley Online Library or from the author.

Conflict of Interest

The authors declare no conflict of interest.

[1] J. A. Rogers, T. Someya, Y. Huang, *Science* **2010**, *327*, 1603.
[2] H. Wu, Y. Huang, F. Xu, Y. Duan, Z. Yin, *Adv. Mater.* **2016**, *28*, 9881.
[3] M. L. Hammock, A. Chortos, B. C. K. Tee, J. B. H. Tok, Z. Bao, *Adv. Mater.* **2013**, *25*, 5997.
[4] A. Chortos, J. Liu, Z. Bao, *Nat. Mater.* **2016**, *15*, 937.
[5] A. Chortos, Z. Bao, *Mater. Today* **2014**, *17*, 321.
[6] D.-H. Kim, N. Lu, R. Ma, Y.-S. Kim, R.-H. Kim, S. Wang, J. Wu, S. M. Won, H. Tao, A. Islam, K. J. Yu, T.-i. Kim, R. Chowdhury, M. Ying, L. Xu, M. Li, H.-J. Chung, H. Keum, M. McCormick, P. Liu, Y.-W. Zhang, F. G. Omenetto, Y. Huang, T. Coleman, J. A. Rogers, *Science* **2011**, *333*, 838.
[7] W. Gao, S. Emaminejad, H. Y. Y. Nyein, S. Challa, K. Chen, A. Peck, H. M. Fahad, H. Ota, H. Shiraki, D. Kiriya, D. H. Lien, G. A. Brooks, R. W. Davis, A. Javey, *Nature* **2016**, *529*, 509.
[8] Y. C. Lai, J. Deng, S. Niu, W. Peng, C. Wu, R. Liu, Z. Wen, Z. L. Wang, *Adv. Mater.* **2016**, *28*, 10024.
[9] W. Guo, P. Zheng, X. Huang, H. Zhuo, Y. Wu, Z. Yin, Z. Li, H. Wu, *ACS Appl. Mater. Interfaces* **2019**, *11*, 8567.
[10] Q. Hua, J. Sun, H. Liu, R. Bao, R. Yu, J. Zhai, C. Pan, Z. L. Wang, *Nat. Commun.* **2018**, *9*, 244.
[11] T. Bu, T. Xiao, Z. Yang, G. Liu, X. Fu, J. Nie, T. Guo, Y. Pang, J. Zhao, F. Xi, C. Zhang, Z. L. Wang, *Adv. Mater.* **2018**, *30*, 1800066.
[12] C. Zhang, S. Liu, X. Huang, W. Guo, Y. Li, H. Wu, *Nano Energy* **2019**, *62*, 164.
[13] S. Wagner, S. Bauer, *MRS Bull.* **2012**, *37*, 207.
[14] C. Wang, C. Wang, Z. Huang, S. Xu, *Adv. Mater.* **2018**, *30*, 1801368.

**ADVANCED
SCIENCE NEWS**
www.advancedsciencenews.com

**ADVANCED
FUNCTIONAL
MATERIALS**
www.afm-journal.de

[15] D. J. Lipomi, M. Vosgueritchian, B. C. Tee, S. L. Hellstrom, J. A. Lee, C. H. Fox, Z. Bao, *Nat. Nanotechnol.* **2011**, *6*, 788.

[16] G. Y. Bae, S. W. Pak, D. Kim, G. Lee, D. H. Kim, Y. Chung, K. Cho, *Adv. Mater.* **2016**, *28*, 5300.

[17] W. Pang, H. Wu, *Adv. Opt. Mater.* **2019**, *7*, 1900329.

[18] A. M. Zamarayeva, A. E. Ostfeld, M. Wang, J. K. Duey, I. Deckman, B. P. Lechêne, G. Davies, D. A. Steingart, A. C. Arias, *Sci. Adv.* **2017**, *3*, e1602051.

[19] S. H. Liu, L. F. Wang, X. L. Feng, Z. Wang, Q. Xu, S. Bai, Y. Qin, Z. L. Wang, *Adv. Mater.* **2017**, *29*, 1606346.

[20] S. Liu, Y. Li, W. Guo, X. Huang, L. Xu, Y.-C. Lai, C. Zhang, H. Wu, *Nano Energy* **2019**, *65*, 104005.

[21] S. Park, H. Kim, M. Vosgueritchian, S. Cheon, H. Kim, J. H. Koo, T. R. Kim, S. Lee, G. Schwartz, H. Chang, *Adv. Mater.* **2014**, *26*, 7324.

[22] S. Wang, L. Lin, Z. L. Wang, *Nano Energy* **2015**, *11*, 436.

[23] F. R. Fan, W. Tang, Z. L. Wang, *Adv. Mater.* **2016**, *28*, 4283.

[24] R. Hinchet, H. J. Yoon, H. Ryu, M. K. Kim, E. K. Choi, D. S. Kim, S. W. Kim, *Science* **2019**, *365*, 491.

[25] G. Zhu, Z. H. Lin, Q. S. Jing, P. Bai, C. F. Pan, Y. Yang, Y. S. Zhou, Z. L. Wang, *Nano Lett.* **2013**, *13*, 847.

[26] S. Wang, Y. Xie, S. Niu, L. Lin, C. Liu, Y. S. Zhou, Z. L. Wang, *Adv. Mater.* **2014**, *26*, 6720.

[27] L. Xu, H. Wu, G. Yao, L. Chen, X. Yang, B. Chen, X. Huang, W. Zhong, X. Chen, Z. Yin, Z. L. Wang, *ACS Nano* **2018**, *12*, 10262.

[28] W. Seung, M. K. Gupta, K. Y. Lee, K.-S. Shin, J.-H. Lee, T. Y. Kim, S. Kim, J. Lin, J. H. Kim, S.-W. Kim, *ACS Nano* **2015**, *9*, 3501.

[29] A. Yu, Y. Zhu, W. Wang, J. Zhai, *Adv. Funct. Mater.* **2019**, *29*, 1900098.

[30] L. Lin, Y. N. Xie, S. H. Wang, W. Z. Wu, S. M. Niu, X. N. Wen, Z. L. Wang, *ACS Nano* **2013**, *7*, 8266.

[31] Y. Yang, H. Zhang, Z. H. Lin, Y. S. Zhou, Q. Jing, Y. Su, J. Yang, J. Chen, C. Hu, Z. L. Wang, *ACS Nano* **2013**, *7*, 9213.

[32] X. Pu, M. Liu, X. Chen, J. Sun, C. Du, Y. Zhang, J. Zhai, W. Hu, Z. L. Wang, *Sci. Adv.* **2017**, *3*, e1700015.

[33] Z. Ren, J. Nie, J. Shao, Q. Lai, L. Wang, J. Chen, X. Chen, Z. L. Wang, *Adv. Funct. Mater.* **2018**, *28*, 1802989.

[34] J. Park, Y. Lee, J. Hong, Y. Lee, M. Ha, Y. Jung, H. Lim, S. Y. Kim, H. Ko, *ACS Nano* **2014**, *8*, 12020.

[35] J. Scheibert, S. Leurent, A. Prevost, G. Debregeas, *Science* **2009**, *323*, 1503.

[36] R. S. Johansson, J. R. Flanagan, *Nat. Rev. Neurosci.* **2009**, *10*, 345.

[37] H. J. Choi, J. H. Lee, J. Jun, T. Y. Kim, S. W. Kim, H. Lee, *Nano Energy* **2016**, *27*, 595.

[38] J. Park, M. Kim, Y. Lee, H. S. Lee, H. Ko, *Sci. Adv.* **2015**, *1*, e1500661.

[39] C. M. Boutry, M. Negre, M. Jorda, O. Vardoulis, A. Chortos, O. Khatib, Z. Bao, *Sci. Rob.* **2018**, *3*, eaau6914.

[40] L. Wang, K. Wang, Z. Lou, K. Jiang, G. Shen, *Adv. Funct. Mater.* **2018**, *28*, 1804510.

[41] Z. Qiu, Y. Wan, W. Zhou, J. Yang, J. Yang, J. Huang, J. Zhang, Q. Liu, S. Huang, N. Bai, Z. Wu, W. Hong, H. Wang, C. F. Guo, *Adv. Funct. Mater.* **2018**, *28*, 1802343.

[42] F. Xu, Y. Zhu, *Adv. Mater.* **2012**, *24*, 5117.

[43] P. Rae, D. Dattelbaum, *Polymer* **2004**, *45*, 7615.

[44] P. Rae, E. Brown, *Polymer* **2005**, *46*, 8128.

[45] M. P. Wolf, G. B. Salieb-Beugelaar, P. Hunziker, *Prog. Polym. Sci.* **2018**, *83*, 97.

[46] X. Z. Jiang, Y. J. Sun, Z. Y. Fan, T. Y. Zhang, *ACS Nano* **2016**, *10*, 7696.

[47] K. Y. Lee, H.-J. Yoon, T. Jiang, X. Wen, W. Seung, S.-W. Kim, Z. L. Wang, *Adv. Energy Mater.* **2016**, *6*, 1502566.

[48] H. Ding, X. Yang, N. Zheng, M. Li, Y. Lai, H. Wu, *Natl. Sci. Rev.* **2018**, *5*, 799.

[49] C. Bartolozzi, L. Natale, F. Nori, G. Metta, *Nat. Mater.* **2016**, *15*, 921.

[50] K. Y. Lee, J. Chun, J. Lee, K. N. Kim, N. R. Kang, J. Y. Kim, M. H. Kim, K.-S. Shin, M. K. Gupta, J. M. Baik, S.-W. Kim, *Adv. Mater.* **2014**, *26*, 5037.

[51] J. A. Fishel, G. E. Loeb, *US Patent 9477909*, **2014**.

[52] Y. Zang, F. Zhang, C.-A. Di, D. Zhu, *Mater. Horiz.* **2015**, *2*, 140.